Contents lists available at ScienceDirect

Sustainable Horizons

journal homepage: www.elsevier.com/locate/horiz





Inertia load reduction for loadoff during floating offshore wind turbine installation: Release decision and ballast control

Can Ma^a, Zhen-Zhong Hu^{a,c}, Xiang Yuan Zheng^a, Zhengru Ren^{a,b,*}

- a Institute for Ocean Engineering, Shenzhen International Graduate School, Tsinghua University, Tsinghua Campus, University Town, Shenzhen 518055, China
- ^b China Institute of Ocean Engineering (Tsing Tao), Qingdao, 266000, China
- ^c Institute for Ocean Engineering, Tsinghua University, Beijing 100084, China

ARTICLE INFO

Keywords: Floating offshore wind turbine Loadoff Nonlinear model predictive control Ballast tank Decision-making support

ABSTRACT

High offshore installation costs are a significant factor limiting the competitiveness of offshore wind energy. One efficient installation approach for floating offshore wind turbines is to preassemble the tower, nacelle, and rotor onshore and perform a single lifting operation to mate the superstructure with the floating foundation at the installation site. It is heavy lifting, due to the weighty payload. At the end of the mating process, a loadoff operation is conducted to transfer the preassembly to the floating foundation. It results in a sudden change in total force acting on the vessel and causes substantial acceleration and potential damage to the mechanism in the onboard nacelles. The magnitude of acceleration of the onboard nacelles can vary greatly at different release instants. In this research, a simplified two-degrees-of-freedom (DOF) (heave and pitch) model is also proposed to account for the heavy lifting process and variable ballast tanks. The sudden payload transfer is approximated using a hyperbolic tangent function to guarantee continuity and differentiability. The loadoff operation consists of the decision-making and vessel-stabilizing phases. Based on the nonlinear model predictive control method, a payload-transfer time selector and anti-pitch ballast controller have been developed to achieve optimal release time decisions and stabilize the vessel after payload release, respectively. Six-DOF simulation results show that the proposed algorithms are capable to a satisfying level of robustness of deciding the optimal payload release time instant, as well as limiting the peak and mean acceleration magnitudes of the onboard nacelles after payload release. The decision-making and control strategies may promote the sustainable energy transformation by extending the operation window and reduce the installation

1. Introduction

Compared to onshore wind energy, offshore wind turbines feature advantages such as a higher wind speed, more stable wind direction, no land area being occupied, and easier electricity transmission to coastal regions (Wu et al., 2019; Sun et al., 2012a). With offshore wind power moving to deeper waters, floating offshore wind turbines (FOWTs) are a promising future application. However, the high levelized cost of the electricity produced remains a constraint at the commercial level (Barlow et al., 2015; Zeng et al., 2023). A recent survey showed that increasing the scale of wind turbines would be an effective means of reducing the cost of the produced electricity (Castro-Santos et al., 2016), but this would mean a higher hub height and a heavier payload for installation. This poses a challenge for lifting and mating the preassemblies. As offshore construction costs account for approximately 10% to 20% of offshore wind energy (Verma et al., 2019), improving

installation efficiency and reducing installation costs are key issues for further commercialization of offshore wind power.

For recently developed FOWTs, the most commonly used installation method is to assemble the wind turbine superstructures onshore or inshore, and transport the preassemblies to the installation site by tugboats (Jiang, 2021), (i.e., wet towing). The FOWT gravity is counteracted by the buoyancy provided by the foundation drainage volume, and the resistance caused by the structure's submerged volume must be overcome in the wet towing process. Studies on wet towing have generally focused on stability and towing resistance (Le et al., 2021; Han et al., 2017; Yan et al., 2021; Gan et al., 2022). Although wet towing avoids complex offshore floating lifting operations, FOWTs can only be towed at limited speeds in low sea states, limiting their applications in far seas.

E-mail address: zhengru.ren@sz.tsinghua.edu.cn (Z. Ren).

Received 20 November 2023; Received in revised form 1 February 2024; Accepted 8 February 2024 Available online 27 February 2024

^{*} Corresponding author at: Institute for Ocean Engineering, Shenzhen International Graduate School, Tsinghua University, Tsinghua Campus, University Town, Shenzhen 518055. China.

An alternative method is to apply a tower-nacelle-rotor preassembly lifting method (Jiang et al., 2018). Preassemblies are secured to the installation vessel by means of railings or flanges and transported to the installation site. Then, one of the preassemblies is lifted by a gripper and mated on a floating foundation. Compared with wet tows, the tower-nacelle-rotor preassembly lifting installation method is more suitable for far seas. Several loads types are important during the preassembly mating operation, such as impact loads between the preassembly and foundation (Verma et al., 2019; Lin et al., 2023), tension in the lifting wires (Messineo and Serrani, 2009; Ren et al., 2023b), and wave-preassembly-foundation interactions (Hu et al., 2017). In order to improve the method, several conceptual studies have been conducted. The time-domain responses of the catamaran-spar-preassembly multibody system are analyzed (Jiang et al., 2018), and schemes using multiple lift wires (Ren et al., 2021b) and a low-height lifting system (Ataei et al., 2023) are proposed to limit the height of the latter. Moreover, to reduce the dynamic response during the mating phase, numerical analysis of SWATH vessels and catamarans installation vessels (Liu et al., 2023a) are investigated. The installation vessel can be specially designed to minimize the probability of interference with waves, depending on the oceanographic datas at the installation site. An automated hydraulic heave compensator is proposed to reduce the relative motion between the preassembly bottom and foundation top during onsite mating operations (Ren et al., 2021a; Zhao et al., 2023). Mechanical coupling structures between the vessel and the floating foundation are considered by Ulstein (2021). A dynamic positioning system equipped on the installation vessel remains close to the desired position on the horizontal plane (Du et al., 2016).

Under allowable sea states, the mating operation is assisted by crews on the floating foundation. The preassembly awaiting release can be considered to be a heavy payload. When the upper gripper is loosened, a large reaction load is generated on the vessel, resulting in a substantial and sudden acceleration at the onboard turbine nacelles, due to the production of the vessel's angular acceleration and long lever arms needed for the hub heights. There is a high risk of damaging the mechanism in the nacelles (Zhang et al., 2015; Verma et al., 2019) (i.e., gearbox Bhardwaj et al., 2019). Therefore, it is necessary to limit the acceleration of the installation vessel, especially the angular acceleration. The stability of the vessel can be improved by increasing the draft and waterline surface areas. However, this causes a higher initial capital cost. Vessel roll reduction equipment such as a bilge keel, fin stabilizer, and ballast tanks can also be used to decrease the angular acceleration magnitude of the vessel. Compared with ballast tanks that are suitable for reducing the roll at all speeds, a fin stabilizer is less effective at low speeds (Fang et al., 2010). Ballast tanks are more suitable for offshore operations when the vessel is relatively stationary. The design of pump systems is constrained by practical limitations such as the size of vessel compartments and ease of maintenance (Lu, 2013). Additionally, for specialized vessels like dredgers, the proportion of pumps in relation to the overall machinery structure of the vessel is relatively higher. The use of active ballast tanks requires consideration of actual physical constraints such as pump flow rates and ballast tank volumes (Wang et al., 2022). A control system based on flow sensors for pumps is also being researched (Rakibuzzaman et al., 2022), which holds technological significance for the real-time control of pumps.

The model predictive control (MPC) is a model-based control algorithm capable of handling complex systems with constraints and dealing with multiple input and output problems (Mayne, 2014). This property makes the MPC method competent for multiple degrees-of-freedom (DOF) systems under certain constraints. The nonlinear model predictive control (NMPC) approach can give feedback to nonlinear systems in real time. Moreover, it can update the observed information and make decisions based on the inputs, which overcomes the short observation signals for waves. Application of MPC has allowed for great progress in the field of ocean engineering, such as with unmanned surface vessels (Gao et al., 2022; Zhang et al., 2022; Feng et al., 2022;

Liu et al., 2022), autonomous underwater vehicles (Dai et al., 2022; Shen et al., 2017, 2019; Li et al., 2023), and offshore wind power (Shah et al., 2021; Ma et al., 2022; Ren et al., 2019; Sun et al., 2022).

Instead of focusing on the relative motion between preassembly and foundation in a mating operation, a release operation has several critical factors, such as the second-impact issues, resulting impact loads, and drift-off. In this paper, the sudden acceleration and resulting inertial loads caused by the payload transfer is of major concern. Algorithms for payload-transfer time selector (PTTS) and anti-pitch ballast controller (APBC) are proposed. By applying the proposed algorithms, the inertial loads acting on the vessel and onboard nacelles can be reduced. The major contributions of this work can be summarized as follows.

- To the best of the authors' knowledge, this work is the first to
 propose a system for decision-making and active control of heavy
 payload loadoff operations. By selecting the release time, the
 wave load and load caused by load transfer are mutually offset.
 An algorithm is proposed for the heavy payload loadoff issue in
 long-crested waves to determine the optimal release time instant.
- Heavy payload loadoff is a stepwise process. By introducing a hyperbolic tangent function, the discrete and discontinuous stepwise function is approximated by a continuous function, enabling calculation of its higher-order derivatives.
- A control algorithm for the ballast tanks was developed to cause a rapid reduction in acceleration at the onboard nacelles after triggering the sudden payload transfer. It can be reasonably assumed that the variation of ballast tank water has little effect on the motions' natural periods.

This study is organized as follows. In Section 2, the heavy payload loadoff issue is described for floating installation vessels. A two DOF simplified control design model is then formulated by considering the loads caused by the release of the preassembly and ballast tanks. In Section 3, an inertial load reduction algorithm (i.e., a combination of the PTTS and APBC algorithms) is proposed to limit the peak and mean acceleration of the onboard nacelles after load off. For this, the direct multiple shooting method is used. In Section 4, simulations are described to verify the algorithms' effectiveness and robustness. In Section 5, the results are summarized.

2. Problem formulation

2.1. System description

This research focuses on a scenario in which a tower, nacelle, and rotor have been preassembled onshore or inshore. A floating installation vessel carries multiple tower-nacelle-rotor preassemblies for offshore installation, as shown in Fig. 1(a). The foundation of the FOWT has been moored. When the installation vessel reaches the installation site, specially designed equipments (such as lower grippers Ulstein, 2021) are used to temporarily couple the installation vessel and floating foundation, aiming to maintain their relative positions in the horizontal plane as consistently. The foundation can slide in the vertical direction surrounded by the gripper. One of the preassemblies is gripped and moved to the stern of the installation vessel. Once the sea state meets the allowable limits, a mating operation is conducted to lift the preassembly onto the floating foundation. With the assistance of the crews on the floating foundation, connect the male connector to the female connector and insert the guide pins of the preassembly into the guide holes of the foundation (see Fig. 1(b)), and the newly-designed connection system can improve the efficiency of inserting and bolting. Once the alignment is complete, the upper gripper is loosened and the mating operation is regarded as being finished. Finally, the crews tighten the nuts to strengthen the connection between the preassembly and the foundation.

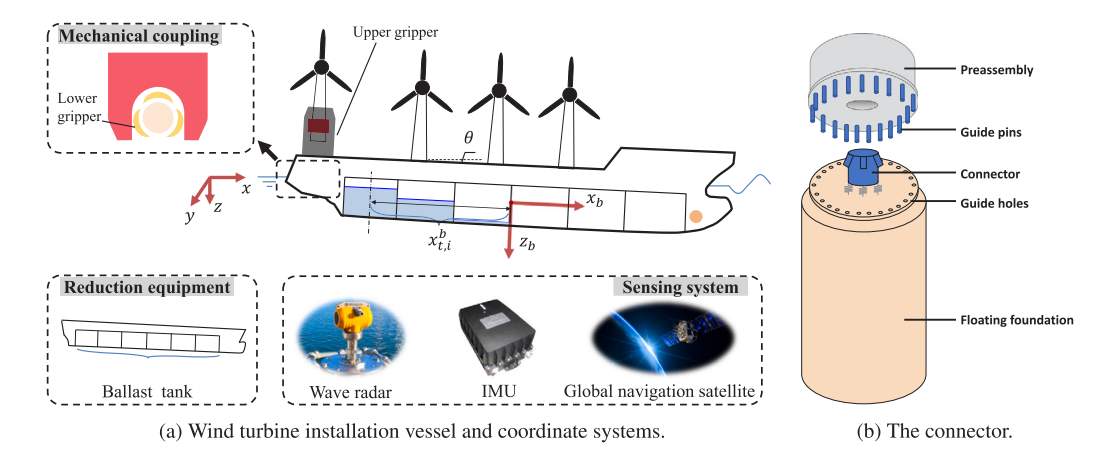


Fig. 1. System setup of an OWT installation vessel with a distributed ballast system.

Releasing the preassembly at different instants results in a variation of the floating installation vessel's responses, further influencing the unreleased preassemblies onboard. Therefore, the operating crews need to be assisted to decide when to loosen the upper gripper based on monitoring systems (Liu et al., 2023b). After the upper gripper is loosened, nuts are slowly tightened by the crews, and the mechanical couplings between the vessel and the FOWT foundation are separated.

Vessel motion is measured by inertial measurement units and a global navigation satellite system. By processing the captured images, a wave radar (i.e., WAMOS 2) can measure and predict wave elevation. Wave loads are estimated by the waves measured by wave radar and the response amplitude operators (RAOs) of the installation vessel. Ballast tanks are used to reduce the vessel's angular acceleration. The ballast tanks are distributed along the longitudinal direction of the vessel and independently connected to the open sea water. The slowly varying current, winds, and second-order wave loads are offset by a dynamic positioning system.

2.2. Heavy payload loadoff issue

The effects of selecting different payload release instants in wave conditions are illustrated in Fig. 2. The total loads acting on the vessel are a superposition of the wave loads, payload gravity, buoyancy, and loads caused by interaction between the gripper and floating foundation. Since the wave loads acting on the vessel are time-varying, different release instants cause different vessel accelerations. The total bending moment at the release instant influences the magnitude and direction of the vessel's angular acceleration. The payload gravity points downwards, and equilibrium is reached if there is a generalized total reacting force pointing upwards after the payload release. If the direction of the reacting payload bending moment is the same as the vessel's angular acceleration direction at the release instant, the angular acceleration of the vessel is amplified. The angular acceleration of the vessel reduces if their directions are different. To limit the huge accelerations generated at the release instant and guarantee structural safety during loadoff, the instant for the step load must be carefully selected.

2.3. System modeling

From the system description, the main components involved in a tower–nacelle–rotor release operation are an installation vessel, tower–nacelle–rotor preassembly, ballast tanks, and the floating foundation that has been moored. The sensing system includes wave radar, inertial measurement units, and a global navigation satellite system. The vessel and preassembly are rigid connected and are treated as rigid bodies together with the floating foundation.

The motions of the floating foundation are not focused on. Two inertial reference frames are defined, both following the right-hand rule

- The north-east-down (NED) coordinate system {n}: The origin point is placed at the free water surface. The x-, y-, and z-axes point to the north, east, and downward normal to the Earth's surface, respectively.
- The body-fixed reference frame $\{b\}$: The origin point is fixed at the vessel mass center. The x^b -, y^b -, and z^b -axes point to the bow, starboard, and downward to the vessel, respectively. The kinetics of the vessel are usually described in $\{b\}$.

The orientation of the vessel with respect to NED is represented by the Euler angle $\Theta_{nb} \in S^3$, including $\operatorname{roll}(\phi)$, $\operatorname{pitch}(\theta)$, and $\operatorname{yaw}(\psi)$. $\eta = [x,y,z,\phi,\theta,\psi]^{\mathsf{T}} \in \mathbb{R}^3 \times S^3$ is the position and rotation vector in $\{n\}$, and $v = [u,v,w,p,q,r]^{\mathsf{T}} \in \mathbb{R}^6$ is the velocity vector in $\{b\}$. The general kinetic model for a heavy-lifting installation vessel (Fossen, 2011) is given by

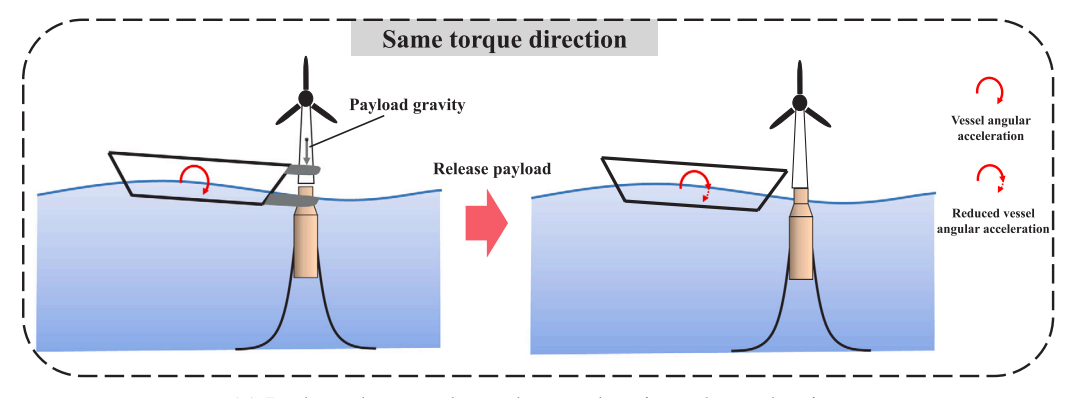
$$(M_{RB}+M_A)\dot{v}+C_{RB}(v)v+C_A(v)v+D(v)v+g(\eta)=\tau_w+\tau_l+\tau_t+\tau_c+\tau_{wind}+\tau_{inter}, \eqno(1)$$

where M_{RB} , M_A , $C_{RB}(v)$, $C_A(v)$, and $D(v) \in \mathbb{R}^{6\times 6}$ are the matrix forms of the rigid-body mass, added mass, rigid-body Coriolis, added mass-induced Coriolis, and damping, respectively. The Coriolis loads are generated due to the rotation of $\{b\}$ about the inertial frame $\{n\}$. Under the small angle assumption, $g(\eta) \approx G\eta$ represents the restoring force where G is the restoring matrix. In addition, the external loads τ_w , τ_l , τ_c , τ_{wind} , and $\tau_{inter} \in \mathbb{R}^6$ denote the loads caused by the waves, heavy payload at the stern of the vessel, ballast tanks, thrusters from the dynamic positioning system, wind, and the interaction between the vessel and floating foundation, respectively.

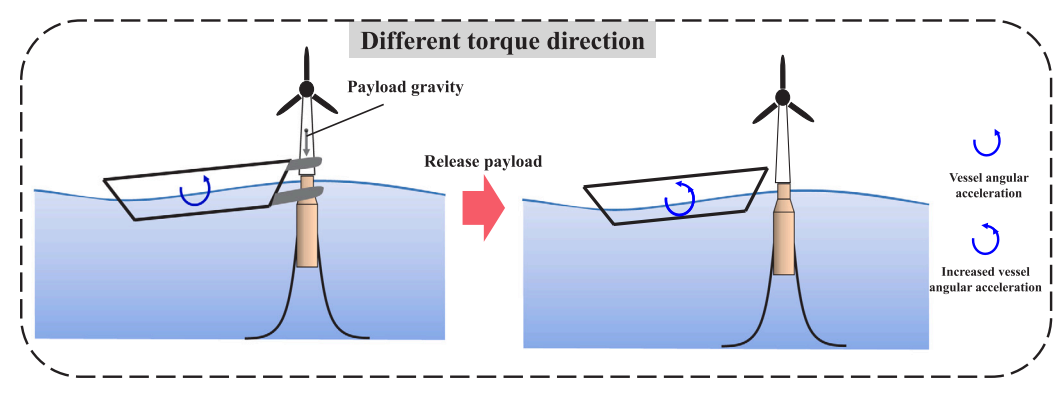
The wave load τ_w is the sum of the first-order wave frequency loads τ_{w1} and the second-order wave drift loads τ_{w2} . The dynamic positioning system thrusters load τ_c is used to compensate for the slow-varying loads, including the wind, current, and the second-order wave drift loads. Since the main research objective was the motion in the vertical plane of the vessel, the dynamic positioning system is not described here in detail.

A load τ_l is employed to describe the load transfer of the towernacelle–rotor preassembly. The waiting-to-release preassembly can be regarded as a rigid body with a lumped mass. The load τ_l depends on the setup. Hereafter, the payload gravity is adopted. Expressed in $\{n\}$, the payload gravity is

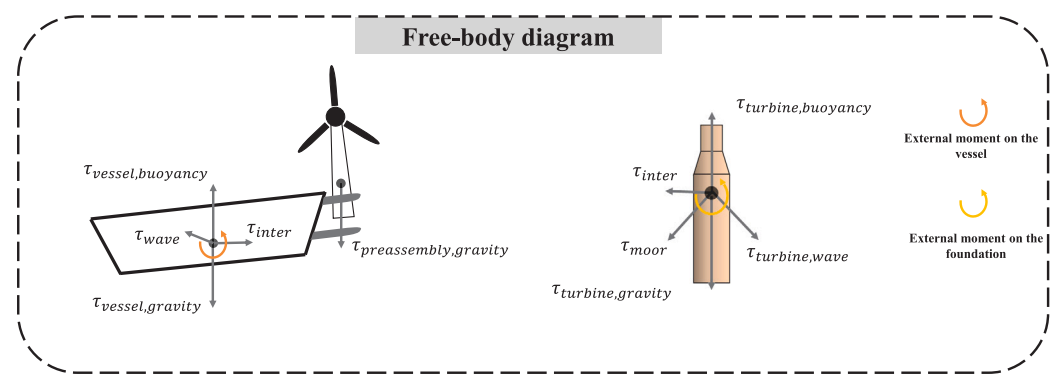
$$F_l^n = \varsigma(t_r) \begin{bmatrix} 0 \\ 0 \\ m_l g \end{bmatrix}, \quad \varsigma = \begin{cases} 1 & \forall \ t < t_r \\ 0 & \forall \ t \ge t_r \end{cases}$$
 (2)



(a) Reduce the vessel angular acceleration when releasing



(b) Increase the vessel angular acceleration when releasing



(c) Free-body diagrams

Fig. 2. (a) and (b): The influence of different payload release instants on the vessel in the waves; (c): Free-body diagrams.

where $\varsigma(t_r)$ is a step factor, m_l is the mass of the preassembly at the stern, g is the gravitational constant, and t_r is the payload release instant. Based on transformations between reference frames, the loads caused by the payload can be expressed as

$$\tau_l = \begin{bmatrix} F_l^b \\ p_l^b \times F_l^b \end{bmatrix} = \begin{bmatrix} R_b^{n\top} F_l^n \\ S(p_l^b) R_b^{n\top} F_l^n \end{bmatrix}, \tag{3}$$

where $R^n_b \in \mathbb{R}^{3 \times 3}$ is the rotation matrix from $\{b\}$ to $\{n\}$, $S(\cdot)$ represents the vector cross-product calculation (i.e., $p_l \times R^{n\top}_b = S(p_l)R^{n\top}_b$), and $p^b_l = [x^b_l, y^b_l, z^b_l]$ is the position of the payload in $\{b\}$. The preassembly is lifted at the mid-longitudinal line of the vessel (i.e., $y^b_l = 0$).

Each tank is equipped with a pump for mobilizing the volume of water inside. The flow rate of the ith pump is expressed as $u_{t,i}$. By increasing or decreasing water in the tanks, a generalized force acts on the installation vessel. The ballast tank force caused by the ith tank

in $\{n\}$ is given by

$$F_{t,i}^{n} = \begin{bmatrix} 0 \\ 0 \\ \rho g \int_{0}^{t} u_{t,i} dt \end{bmatrix}, \quad i = 1, 2...n_{t},$$
 (4)

where $F^n_{t,i}$ is the force vector caused by the ith tank, n_t represents the amount of the tanks, and $u_{t,i}$ denotes the ith pump flow rate. The overall loads generated by the tanks τ_t in $\{b\}$ is

$$\tau_{t} = \begin{bmatrix} F_{t}^{b} \\ p_{t,i}^{b} \times F_{t}^{b} \end{bmatrix} = \sum_{i=1}^{n_{t}} \begin{bmatrix} R_{b}^{n \top} F_{t,i}^{n} \\ S(p_{t,i}^{b}) R_{b}^{n \top} F_{t,i}^{n} \end{bmatrix},$$
 (5)

where $p_{t,i}^b = [x_{t,i}^b, y_{t,i}^b, z_{t,i}^b]^{\mathsf{T}}$ is the center of the water in the ith tank. To simplify the calculation, the value of $p_{t,i}^b$ is assumed to be constant.

The amplitude of the acceleration at the turbine nacelle is related to the vessel's acceleration and hub height. Relationships between the

turbine nacelle and vessel motions are given by

$$p_{n,i}^{n} = p_{s}^{n} + R_{b}^{n} l_{n,i}^{b}, (6a)$$

$$\dot{p}_{n,i}^{n} = \dot{p}_{s}^{n} + R_{b}^{n} S(\omega) l_{n,i}^{b},$$
 (6b)

$$\ddot{p}_{n,i}^{n} = \ddot{p}_{s}^{n} + R_{b}^{n} S^{2}(\omega) l_{n,i}^{b} + R_{b}^{n} S(\alpha) l_{n,i}^{b}, \tag{6c}$$

where $p_{n,j}^n = [x_{n,j}^n, y_{n,j}^n, z_{n,j}^n]^{\mathsf{T}}$ represents the position of the jth turbine nacelle in $\{n\}$, $p_s^n = [x_s^n, y_s^n, z_s^n]^{\mathsf{T}}$ means the position of the installation vessel in $\{n\}$, $l_{b,j}^n$ is the relative distance from the vessel's gravity center to the jth turbine hub, and ω and α are the angular velocity and angular acceleration of the installation vessel, respectively.

2.4. Simplified control design model

The vessel model of Eq. (1) is difficult to use in a control design, due to its high complexity. Since the payload is released at the stern and the inertia loads in the vertical plane are of larger magnitudes, the pitch motion of the vessel is the DOF of highest importance. The release of the payload and changes in the tanks' water volumes directly influence the heave motion of the installation vessel. Therefore, two simplified models are proposed for the control design, wherein the dominant DOFs are heave and pitch and less important DOFs are ignored. The 6DOF model will be used in numerical simulations to verify the controller designed according to the simplified 2DOF model. To establish the control algorithm, the following necessary assumptions are proposed.

- For the sake of simplification, only long-crested waves are considered in this study.
- Wave loads can be accurately predicted within 5 to 10 s. This
 can be achieved through several wave-prediction methods, such
 as machine learning (Ma et al., 2021), sparse regression (Ren
 et al., 2023a), and image processing (Borge et al., 2004). To avoid
 repetition, the algorithms are not presented here.
- The free surface effects of the water in the tanks are negligible.
- Variations in vessel buoyancy and gravity center caused by the changes in water volume in the ballast tanks and payload release are neglected. Also, the impact on the vessel hydrostatics is also disregarded.

The second-order wave drift loads τ_{w2} and wind loads τ_{wind} are offset by the dynamic positioning system τ_c . The interaction loads between the vessel and the foundation act only in the horizontal plane, which also can be offset by the dynamic positioning system. Therefore, they are removed from the simplified model. The wave elevation is the superposition of several harmonic wave components.

To avoid repetition, the position and velocity vectors are defined by $\eta_s = [z, \theta]^{\mathsf{T}}$ and $v_s = [w, q]^{\mathsf{T}}$, respectively. The ballast tanks are turned off during the decision-making phase to make full use of the wave-induced loads, in order to compensate for the inertial loads. To achieve payload release decision-making, and ballast tank control, the resulting simplified state-space equation for the installation vessel is divided into the following forms:

(1) Simplified control design model for release decision-making:

$$\begin{split} \dot{\eta}_{s} &= \begin{bmatrix} \cos(\theta) & 0 \\ 0 & 1 \end{bmatrix} v_{s}, \\ \dot{v}_{s} &= \begin{bmatrix} m + a_{33} & 0 \\ 0 & I_{y} + a_{55} \end{bmatrix}^{-1} (\sum_{k=1}^{n_{f}} \rho g \sqrt{2S(\omega_{k})\Delta\omega} \\ \begin{bmatrix} \text{RAO}_{3,k} \cos(\omega_{k}t + \varepsilon_{k} + \varphi_{3,k}) \\ \text{RAO}_{5,k} \cos(\omega_{k}t + \varepsilon_{k} + \varphi_{5,k}) \end{bmatrix} + \varsigma(t_{r})F_{l} \begin{bmatrix} \cos(\theta) \\ -z_{l} \sin(\theta) - x_{l} \cos(\theta) \end{bmatrix} \\ &- \begin{bmatrix} G_{33} & G_{35} \\ G_{53} & G_{55} \end{bmatrix} \eta_{s} - \begin{bmatrix} D_{33} & 0 \\ 0 & D_{55} \end{bmatrix} v_{s} \\ &- \begin{bmatrix} 0 & a_{1} - m \cdot u \\ a_{1} + m \cdot u & 0 \end{bmatrix} v_{s}), \end{split}$$
(7b)

$$a_1 = X_{ii}w + X_{ij}q, (7c)$$

where n_f is the number of wave components, ω_k and ε_k are the frequency and initial phase of the kth frequency of waves, respectively, $\Delta\omega$ is the frequency sampling interval, RAO $_{dof,k}$ is the kth force transfer RAO at a specific DOF, $\varphi_{dof,k}$ is the kth phase transfer RAO at a specific DOF, $S(\omega_k)$ is the wave power spectrum, F_l is the force acting on the gripper in z^b which can be measured by attached force sensor. a_{33} and a_{55} are added mass caused by the heave and pitch motions, respectively, G_{33} , G_{35} , G_{53} , and G_{55} are restoring factors, D_{33} and D_{55} are damping factors, and for instance $X_{\hat{w}}$ is the hydrodynamic added mass force X along the z-axis due to an acceleration \hat{w} in the z direction.

(2) Simplified control design model for ballast control:

$$\begin{split} \dot{\eta}_{s} &= \begin{bmatrix} \cos(\theta) & 0 \\ 0 & 1 \end{bmatrix} v_{s}, \\ \dot{v}_{s} &= \begin{bmatrix} m + a_{33} & 0 \\ 0 & I_{y} + a_{55} \end{bmatrix}^{-1} (\sum_{k=1}^{n_{f}} \rho_{g} \sqrt{2S(\omega_{k})\Delta\omega} \\ \begin{bmatrix} \text{RAO}_{3,k} \cos(\omega_{k}t + \varepsilon_{k} + \varphi_{3,k}) \\ \text{RAO}_{5,k} \cos(\omega_{k}t + \varepsilon_{k} + \varphi_{5,k}) \end{bmatrix} + \sum_{i=1}^{n_{t}} \rho_{g} \int_{0}^{t} u_{t,i} dt \\ \begin{bmatrix} \cos(\theta) \\ -z_{t,i} \sin(\theta) - x_{t,i} \cos(\theta) \end{bmatrix} - \begin{bmatrix} G_{33} & G_{35} \\ G_{53} & G_{55} \end{bmatrix} \eta_{s} - \begin{bmatrix} D_{33} & 0 \\ 0 & D_{55} \end{bmatrix} v_{s} \\ - \begin{bmatrix} 0 & a_{1} - m \cdot u \\ a_{1} + m \cdot u & 0 \end{bmatrix} v_{s}), \end{split}$$
 (8b)

$$\dot{V}_{t,i} = u_{t,i}, \quad i = 1, \dots, n_t,$$
 (8c)

$$a_1 = X_{\dot{w}}w + X_{\dot{a}}q. \tag{8d}$$

After finishing the payload release operation, the load acting on the vessel by the payload is always zero, so the stepwise load is no longer considered in the Eq. (8). Although the vessel's RAOs change with the volumes of ballast water, the displacement variation is not significant, resulting in an insignificant difference in RAOs. Additionally, changing RAOs during simulations is very difficult to implement in the currently available numerical codes. Hence, constant RAOs are applied.

$2.5. \ \ Continuous \ differential \ approximation \ of \ the \ step \ release \ process$

The loads of the lifted payload τ_l during the release process are stepwise and discontinuous at the release instant. The sudden jump causes singularity problems in control designs. To ensure that loads of the lifted payload τ_l are sufficiently continuously differentiable, a hyperbolic tangent function is employed to approximate the step factor ζ_1

$$\varsigma(t_r) \approx \frac{1}{2} \tanh(\frac{t_r - t}{\kappa}) + \frac{1}{2},\tag{9}$$

where κ is a positive small number. Fig. 3 shows the effects of different values of κ . The difference between ς and its approximation is reduced by decreasing the value of κ .

2.6. Problem statement

The elements in the state variable $\mathfrak x$ and control variable $\mathfrak u$ are constrained in practice. Therefore, the following constraints are considered in the control design.

C1: The initial value at the t_0 moment is obtained by real-time monitoring (i.e., $x(t_0)$ is known).

C2: The pump flow rate is limited by its rated power (i.e., $\underline{u}_{t,i} \leq u_{t,i}(t) \leq \overline{u}_{t,i}$), where $\underline{u}_{t,i}$ and $\overline{u}_{t,i}$ denote the lower and upper flow rates of the *i*th pump, respectively.

C3: The volume of the ballast tank is limited (i.e., $0 \le V_{t,i}(t) \le \overline{V}_{t,i}$), where $\overline{V}_{t,i}$ denotes the maximum volume of the *i*th ballast tank.

To achieve a safe and efficient release operation, the following two issues need to be resolved.

1. Limit the max peak acceleration of the onboard nacelles.

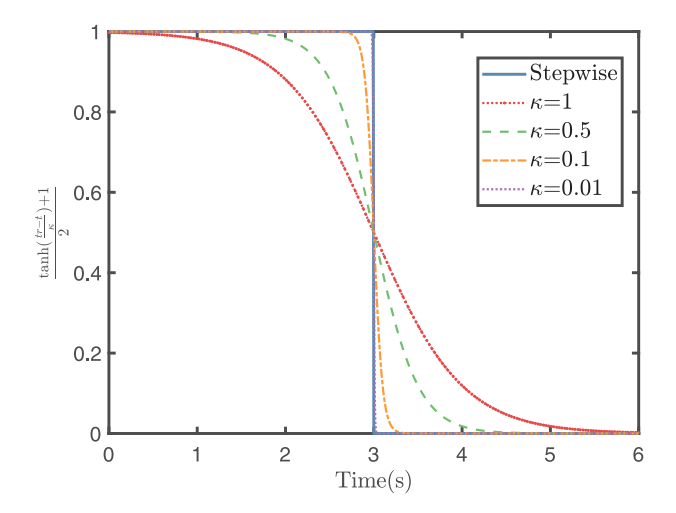


Fig. 3. Approximation of the step factor ς with different κ ($t_r = 3$ s).

The sudden heavy-lifting release operation generates a generalized step reaction load τ_l that risks damaging the mechanism in the onboard nacelles. The amplitudes of the wave-induced loads are much smaller than that of τ_l . Since the direction of the wave loads changes periodically, different release time instants cause the wave loads to be superimposed on or cancel out the step loads of the lifted payload. As much as possible, the payload release instant t_r , should be selected to compensate for the wave loads with the step loads of the lifted payload τ_l to protect the mechanism in the nacelles. Hence, the control objective is to find the optimal release instant t_r^* , such that

$$\max_{i}(|\ddot{p}_{n,j}^{n}(t_{r}^{*})|) \leq \overline{a}, \quad j = 1.....n_{t}, \tag{10}$$

where \bar{a} is the nacelle acceleration safety threshold given by the wind turbine manufacturers. Moreover, the $\ddot{p}_{n,j}^n(t_r^*)$ is calculated via Eqs. (6) and (7).

2. Minimize the mean acceleration at the onboard nacelles.

Besides the release time instant, there is a significant need to reduce the nacelle acceleration over a relatively long term. A smaller mean nacelle acceleration means a smaller amplitude of motion and higher degree of vessel stability. The ballast tanks are actively controlled after execution of the release operation. By controlling the pump flow rate \mathfrak{u}^* , the ballast tank load τ_t compensates for the τ_{w1} to the maximum degree after the payload release. Hence, the control objective is to minimize the mean nacelle acceleration amplitude in a period $[t_r^*,t_r^*+T]$ by calculating the ballast tank pump flow rate \mathfrak{u}^* , such that

$$u^* = \arg\min_{u} \sum_{i=1}^{n_t} \frac{\int_T \|\ddot{p}_{n,j}^n(t)\|^2 dt}{T},$$
(11)

where $\ddot{p}_{n,j}^n(t)$ is calculated via Eqs. (6) and (8). The decision-support algorithm is helpful for the operating crews to plan a safe payload release operation by deciding the optimal time instant in advance or providing signals to the automatic system. Additionally, the oscillation of the vessel after release can quickly be reduced by controlling the ballast pumps. It is important to note that the primary design of the ballast tanks requires practical considerations based on the vessel design, pump capacity, and other dominant factors.

3. Decision making and control design

3.1. Discretization of state-space equations

The proposed system is a multiple-input multiple-output problem with several constraints that is suitable for solving with an NMPC approach. The control inputs are calculated by solving a finite timedomain optimal control problem. The continuous optimal control problem must first be discretized into a nonlinear programming problem to perform numerical calculations.

The direct multiple shooting method is applied to achieve the discretization requirement. The principle of the direct multiple shooting method is shown in Fig. 4. A time horizon $[t_0, t_0 + T]$ is divided into N intervals with the constant sample time $\delta t = T/N$, where t_0 is the starting time, T represents the length of the predicted time horizon, and N is the number of intervals. The state-space equations in each interval can be independently integrated. The initial predicted state and control variables at each interval are the variables to be calculated. For ease of expression, the initial predicted state and control variables are defined as s(k) and r(k), respectively. To retain the continuity of the predicted state variables, the equation constraints are given by

$$g(k+1) = f(s(k), r(k)),$$
 (12a)

$$f(s(k), r(k)) = s(k+1),$$
 (12b)

where k is the discrete time-step of the subinterval, f(s(k), r(k)) refers to the discrete time integrator of Eq. (7) or (8), and $\mathfrak{x}(k+1)$ denotes the final predicted state variables at the k+1 moment. The above equation can be interpreted as that the initial state variable s(k+1) at the moment k+1 is equal to the state variable f(s(k), r(k)), calculated by Eq. (7) or (8). Moreover, the state variables are smooth, due to the equation constraints in Eq. (12).

3.2. Cost function of the model predictive control

The running cost is given to reflect the importance of each state variable, control variable, and other parameters at every spacial time grid. Due to the use of the multiple shooting method, the solution becomes an optimization of the running cost function with respect to s(k) and r(k). The most important items can be controlled first by setting high weights for the corresponding parts in the running cost $\ell(s(k), r(k))$.

3.2.1. Cost function in the PTTS algorithm

To derive the PTTS algorithm and make payload release decisions, the running cost is defined as

$$\mathcal{E}_1(s_1(k)) = \sum_{i=1}^{n_n} \|\vec{p}_{n,i}^n(k)\|_{\mathfrak{Q}}^2, \quad k = 0, 1, \dots, N_1,$$
(13)

where $\|\ddot{p}_{n,i}^n(k)\|_{\mathfrak{Q}}^2 = \ddot{p}_{n,i}^n(k)^{\mathsf{T}}\mathfrak{Q}\ddot{p}_{n,i}^n(k)$, \mathfrak{Q} is a diagonal positive weight matrix, $s_1 = [z,\theta,w,q]^{\mathsf{T}}$ is the initial predicted state variable for the simplified control design model without ballast tanks, N_1 is the prediction step, δt_1 is the interval sampling time, and n_n is the number of onboard nacelles. Moreover, the values of $\ddot{p}_{n,i}^n(k)$ in Eq. (13) are calculated by Eqs. (6) and (7).

The cost function is the summation of the running cost $\ell_1(s_1(k))$ across the entire prediction horizon, given by

$$\min_{s_1,t_r} \qquad L_1(s_1,t_r) = \sum_{k=t_0}^{t_0+N_1\delta t_1} \mathcal{E}_1(s_1(k)) + \beta |t_r|^2 + E_N(s_1(N_1)), \tag{14a} \label{eq:14a}$$

s.t.
$$\mathfrak{x}_1(0) - s_1(0) = 0,$$
 (14b)

$$f_1(s_1(k)) = s_1(k+1),$$
 (14c)

$$0 \le t_r \le N_1 \delta t_1,\tag{14d}$$

where $L_1(s_1,t_r)$ is the cost function of the decision-making operation, the value of β influences selection of the release instant, $E_N(s_1(N_1))$ is the end time contribution, which is calculated by $E_N(s_1(N_1)) = \|s_1(N_1)\|_{\mathfrak{P}}^2$, and \mathfrak{P} is a positive-definite weighting matrix. The payload release instant t_r is limited within the forecast time period.

C. Ma et al. Sustainable Horizons 10 (2024) 100096

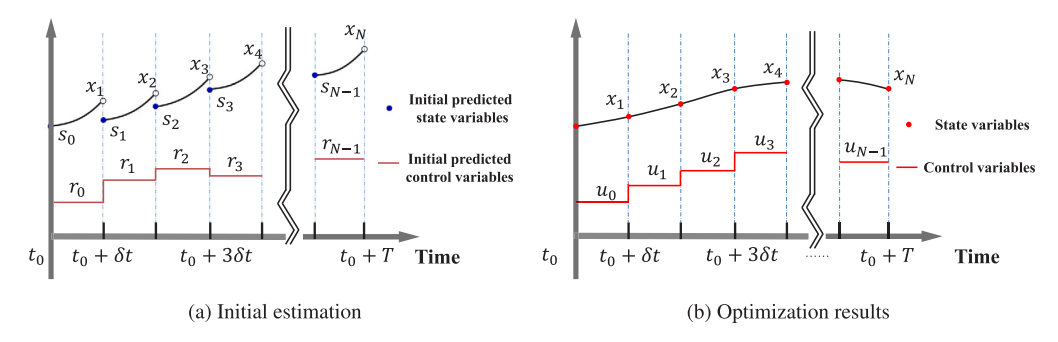


Fig. 4. The principle of the direct multiple shooting method.

3.2.2. Cost function in the APBC algorithm

The running cost $\ell_2(s_2(k), r_2(k))$ of APBC is given by

$$\ell_2(s_2(k), r_2(k)) = \sum_{i=1}^{n_n} \|\ddot{p}_{n,i}^n(k)\|_{\mathfrak{Q}}^2 + \|r_2(k)\|_{\mathfrak{R}}^2, \quad k = 0, 1, \dots, N_2,$$
 (15)

where $\mathfrak R$ and $\mathfrak Q$ are the diagonal positive weighting matrices, the weight matrix $\mathfrak R$ allows for the distribution of the pump energy, allowing for larger $\mathfrak R$ matrix factors for ballast tanks further away from the middle of the vessel, $s_2 = [z,\theta,w,q,V_{t,1},V_{t,2}...,V_{t,n_t}]^{\mathsf{T}}$ is the initial predicted state variable for the simplified control design model without a payload, $V_{t,i}$ is the water volume of the ith ballast tank, and $r_2 = [u_{t,1},u_{t,2},\ldots,u_{t,n_t}]^{\mathsf{T}}$ is the initial predicted control variable. The state variable s_2 and control variable r_2 are limited by the physical limits of the equipment. The vector $p_{n,i}^n(k)$ in Eq. (15) is calculated by the Eqs. (6) and (8).

Also, the cost function is the summation of the running cost $\ell(s_2(k), r_2(k))$ across the entire prediction horizon, given by

$$\min_{s_2, r_2} L_2(s_2, r_2) = \sum_{k=0}^{N_2 - 1} \ell_2(s_2(k), r_2(k)) + E_N(s_2(N_2)),$$
 (16a)

s.t.
$$\mathfrak{x}_2(0) - \mathfrak{s}_2(0) = 0$$
, (16b)

$$f_2(s_2(k), r_2(k)) = s_2(k+1),$$
 (16c)

$$u \le r_2(k) \le \overline{u}, \quad k = 0, 1, \dots, N_2 - 1,$$
 (16d)

$$\underline{x} \le s_2(k) \le \overline{x}, \quad k = 1, 2, \dots, N_2,$$
 (16e)

where $L_2(s_2,r_2)$ is the cost function of the ballast tank control operation, $\underline{u}=[\underline{u}_{t,1},\underline{u}_{t,2}...,\underline{u}_{t,n_t}], \overline{u}=[\overline{u}_{t,1},\overline{u}_{t,2}...,\overline{u}_{t,n_t}], \underline{x}=[-\infty,-\infty,-\infty,-\infty,0,0,\dots,0],$ and $\overline{x}=[+\infty,+\infty,+\infty,+\infty,\overline{V}_{t,1},\overline{V}_{t,2},...,\overline{V}_{t,n_t}].$ By minimizing the cost function, the state and control variables of the final iteration can be obtained.

3.3. Overview of the inertial load reduction algorithm

The logic of the inertial load reduction algorithms is shown in Fig. 5. The plant can be an actual vessel, scaled model, or high-fidelity simulation model. Motion sensors and wave radar are used to obtain the real-time state variables of the vessel and sense waves, respectively. To select the optimal release time instant for the preassembly at the stern, a PTTS can be used to identify the optimal release instant based on the wave forecasts. A payload release decision flag c is set to an initial value of 1, meant to execute the PTTS algorithm first. The flag is used to receive a signal regarding whether the payload is released and decide which algorithm to execute. An APBC is set up to stabilize the installation vessel after releasing the payload by controlling the flow rate of each water tank distributed along the length direction. The APBC algorithm can minimize the peak acceleration of the onboard wind turbine nacelles after the payload release.

The entire process is divided into decision-making and vesselstabilizing phases. The inertial load reduction algorithm is a combination of the PTTS and APBC algorithms, established to guarantee the loadoff operation within the operational time window $[t_{decition,start}, t_{operation,end}]$ (see Fig. 6 and Algorithm 1). If the current time t reaches the beginning of the decision-making time $t_{decision,start}$ and the value of the release decision flag remains c=1, the PTTS algorithm is executed. The control algorithms can be integrated into the vessel's operation center to assist the crews or to conduct automatic scheduling in executing payload release operations. The PTTS algorithm calculates the locally optimal release instant t_r^* in the next time grid and decides whether to accept the release instant t_r^* based on the preset release conditions. If the release condition is satisfied, the calculated t_r^* is accepted and the value of the release decision flag becomes c=0. Otherwise, the release decision flag remains c=1 and the PTTS algorithm continues at the next sample time instant. The iteration lasts until the end of the decision-making time $t_{decision,end}$.

After finishing the preassembly loadoff, acceleration of the vessel and turbine nacelle increases steeply. To achieve rapid recovery after release, the APBC algorithm (based on the principle of the NMPC) is proposed. After the payload transfer is executed (i.e., c=0), the APBC algorithm starts at each sample time to control the ballast tank flow rate u*. The pump flow rates and ballast tank volumes are the constraints on the APBC. By roll-optimizing the pump flow rate of each ballast tank, the mean acceleration of the wind turbine nacelles is limited until operation termination $t_{operation.end}$.

Algorithm 1 Inertial load reduction algorithm

```
Input: z(t), \theta(t), \omega(t), q(t), V_{t,1}(t), V_{t,2}(t), ... V_{t,n}(t);
        Parameters: t_{decision,start}, t_{decision,end}, t_{operation,end}, \overline{a}; c \leftarrow 1;
  1: while t \le t_{operation,end} do
  2:
              switch t do
             case t_{decision,start} \le t \le t_{decision,end}
if c = 1 then
  3:
  4:
                                \begin{split} &(t_r^*, \ddot{p}_{n,j}^n) \leftarrow \arg\min L_1 \ (z(t), \theta(t), \omega(t), q(t)) \\ &\mathbf{if} \ \max(|\ddot{p}_{n,j}^n(t_r^*)|) \leqslant \overline{a}, \end{split} 
  5:
  6:
                                        Execute the t_{*}^{*}, c \leftarrow 0
  7:
  8:
                               end if
  9:
                      else
10:
                               \mathfrak{u}^*(t) \leftarrow \arg \min L_2(z(t), \theta(t), \omega(t), q(t), V_{t,1}(t), ..., V_{t,n_t}(t))
11:
                       end if
12:
              \textbf{case} \quad t_{decision,end} < t \leqslant t_{operation,end}
                       if c = 0 then
13:
                               \mathfrak{u}^*(t) \leftarrow \arg\min L_2\left(z(t), \theta(t), \omega(t), q(t), V_{t,1}(t), ..., V_{t,n_t}(t)\right)
14:
15:
                       end if
              end switch
16:
              t = t + \Delta t
17:
18: end while
```

The acceleration magnitudes for the onboard turbine nacelles vary with the selection of release time. The PTTS algorithm is executed for each sample time during the decision-making period. The local optimal release time in the prediction steps N_1 can be calculated by solving the optimal question at the current sample time point. The sample time δt_1 can be set higher to achieve a longer decision horizon. However, a

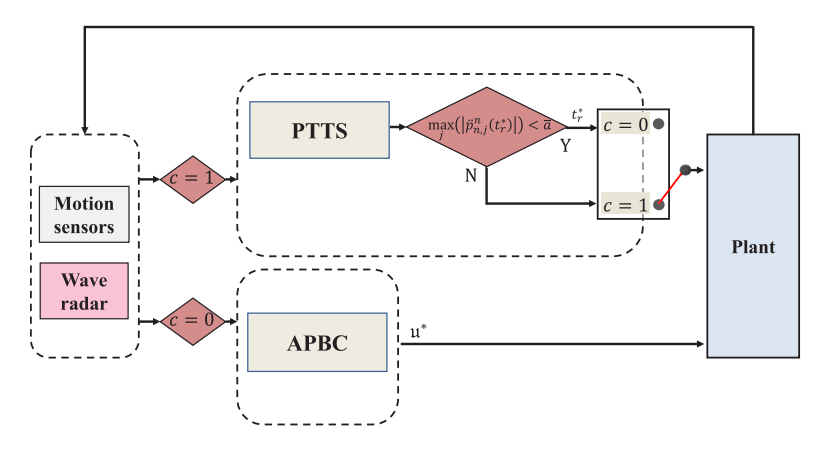


Fig. 5. Block diagram of the load reduction scheme.

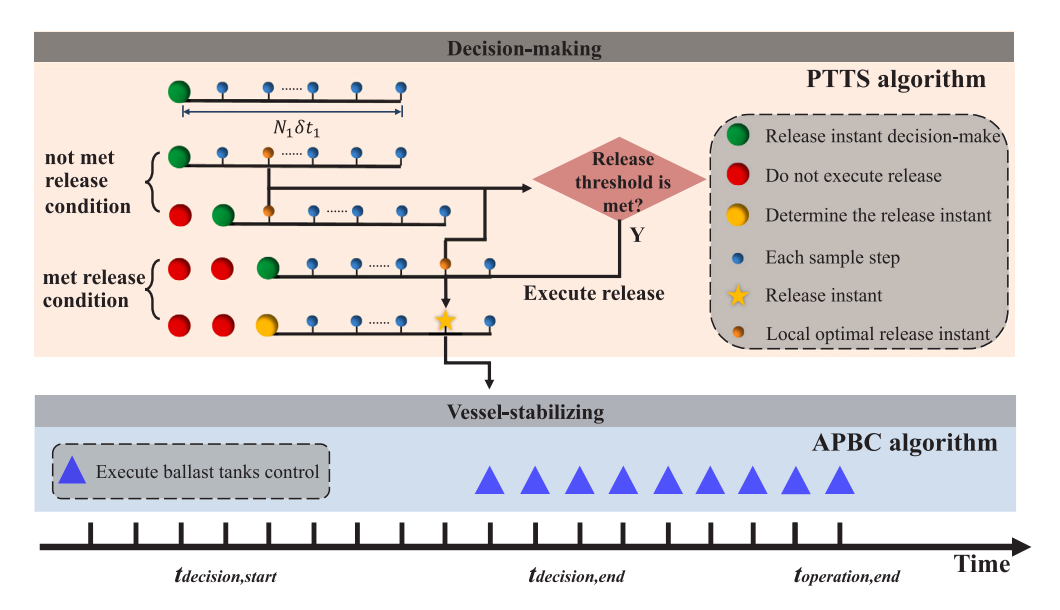


Fig. 6. Control strategy for the PTTS and APBC algorithms.

too large value of δt_1 results in low resolution and missing some of the proper payload release instants during the wind turbine construction process. Moreover, a higher number of prediction steps N_1 results in a longer computation time. Due to the transient nature of the release operation, invoking the APBC algorithm using ballast tanks are unable to reduce the accelerations at the moment of release. The parameter δt_2 represents the sampling time step of the APBC algorithm, and a small δt_2 is required to counteract the wave loads associated with shorter waves. However, utilizing a smaller sampling time step, on the other hand, results in a larger computational workload.

4. Simulation

4.1. Simulation overview

The simulations were conducted in 6DOF using Matlab/Simulink, MSS, MARIN (Ren et al., 2018), and the Casadi toolboxes (Andersson et al., 2019). Based on the simplified control design model, the PTTS and APBC algorithms were used to select the payload release instant t_r^* and control the ballast tank pump flow rate $\mathfrak{u}^*(t)$, respectively. To improve simulation accuracy, the simulation verification model considered the fluid memory effects, cross-flow drag, and surge resistance, in order to characterize the system.

Wamit calculated the hydrodynamic parameters for the installation vessel without considering the interferences of the spar foundation. The vessel's hull shape was simplified to a regular barge shape. The principle parameters of the vessel and the main parameters of the total system are listed in Table 1. In the simulations, there were six ballast tanks distributed along the length of the vessel (i.e., $n_t = 6$). The max pump rate magnitude $\overline{u}_{t,i}$ was set as 10 m³/s, and the ballast tanks' maximum volume $\overline{V}_{t,i}$ is 180 m³. By adding or reducing the volume of ballast water in each tank, additional forces and bending moments could be generated for the vessel. Long-crested waves were considered in the simulations, and the waves propagated against the bow. Each simulation lasted for 800 s. To ensure computational efficiency, the value of the prediction steps N_1 in the PTTS algorithm and N_2 in the APBC algorithm were set to 10. The sampling intervals δt_1 and δt_2 were both set to 0.5 s.

4.2. Influence of different payload release instants

Firstly, a simulation, considering the release of the payload process in the absence of waves, was conducted to understand the system dynamic behavior and assess the reliability of the simulation method. The simulation results are shown in Fig. 7, and the initial 500 s were removed. The maximum acceleration of the nacelles onboard sharply increased after the release of the payload, and it took about 50 s to dampen out. The vessel draft was reduced by approximately 0.4 m after the payload release from the stern, and the vessel no longer had a

Table 1
Main parameters for the simulations.

Part	Parameter	Value	Unit
	Vessel length	150	m
	Vessel width	33	m
Vessel	Vessel draft	9	m
vessei	Vessel mass m	4.236×10^4	ton
	Moment of inertia pm the y^b -axis I_y	6.948×10^{10}	kg m ²
	Gravity center position of the vessel	(0,0,-1)	m
	Number of ballast tanks	6	-
	Position of ballast tank centers on the x-axis $x_{t,i}$	60, 40, 20, -20, -40, -60	m
Ballast system	Position of ballast tank centers on the z-axis $z_{t,i}$	-8.25	m
	Ballast tank maximum volume \overline{V}_{tn}	180	m^3
	Minimum and maximum pump rates $(\underline{u}_{t,n_t}, \overline{u}_{t,n_t})$	(-10,10)	m^3/s
Mated massesmbly	Payload mass m ₁	2000	ton
Mated preassembly	Gravity center position of the payload on the x-axis x_1	-100	m
(payload)	Gravity center position of the payload on the z-axis z_l	-80	m
	Number of preassemblies n_n	3	-
Onboard preassemblies	Position of the <i>j-th</i> preassembly on the x-axis $x_{n,i}^n$	70,0,-70	m
	Position of the preassemblies on the z-axis $z_{n,i}^n$	-160	m

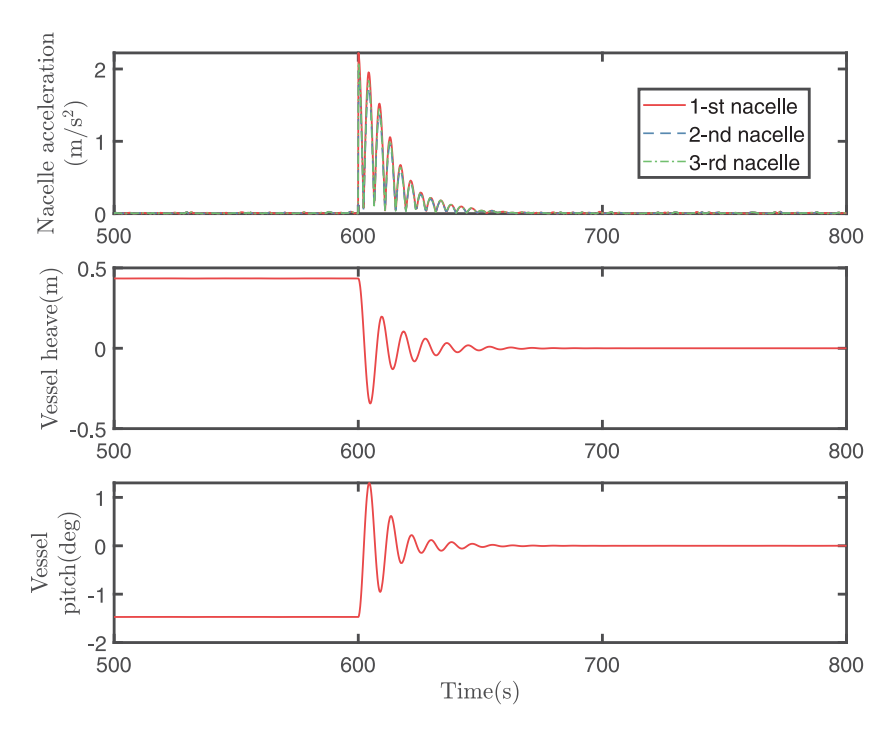


Fig. 7. Motions after releasing the payload in the absence of waves.

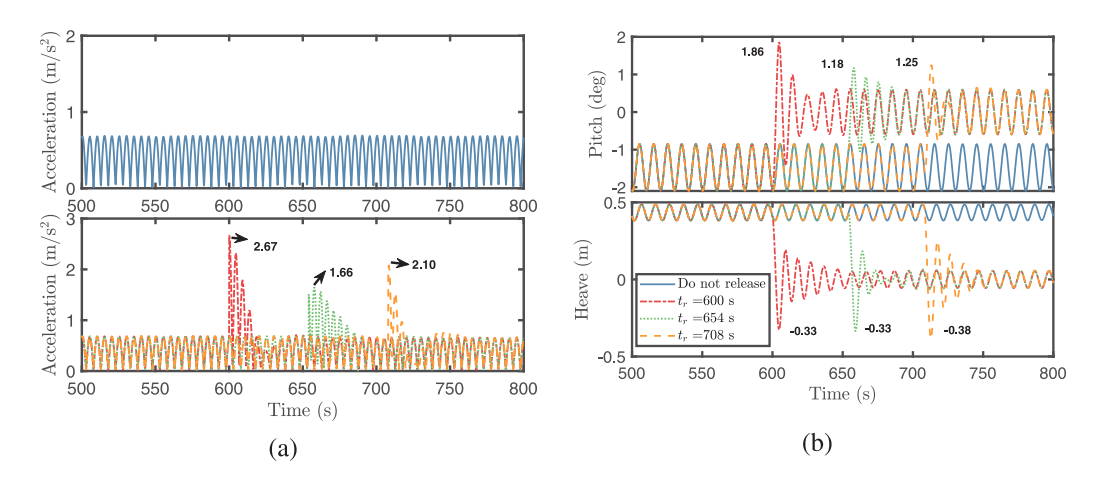
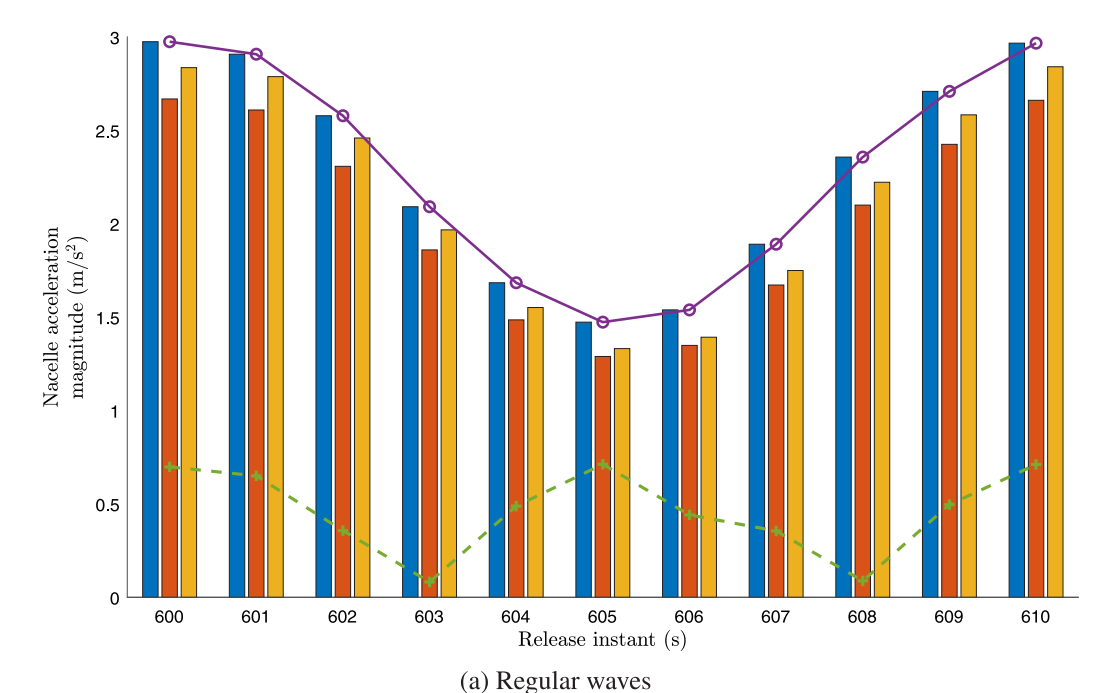


Fig. 8. Simulations of the vessel's motion and nacelle acceleration under different payload release instants. (a) Acceleration magnitude of the nacelle placed in the middle of the vessel dock $|\vec{p}_n^n\rangle$ without payload released and with payload released and (b) motion of the vessel.



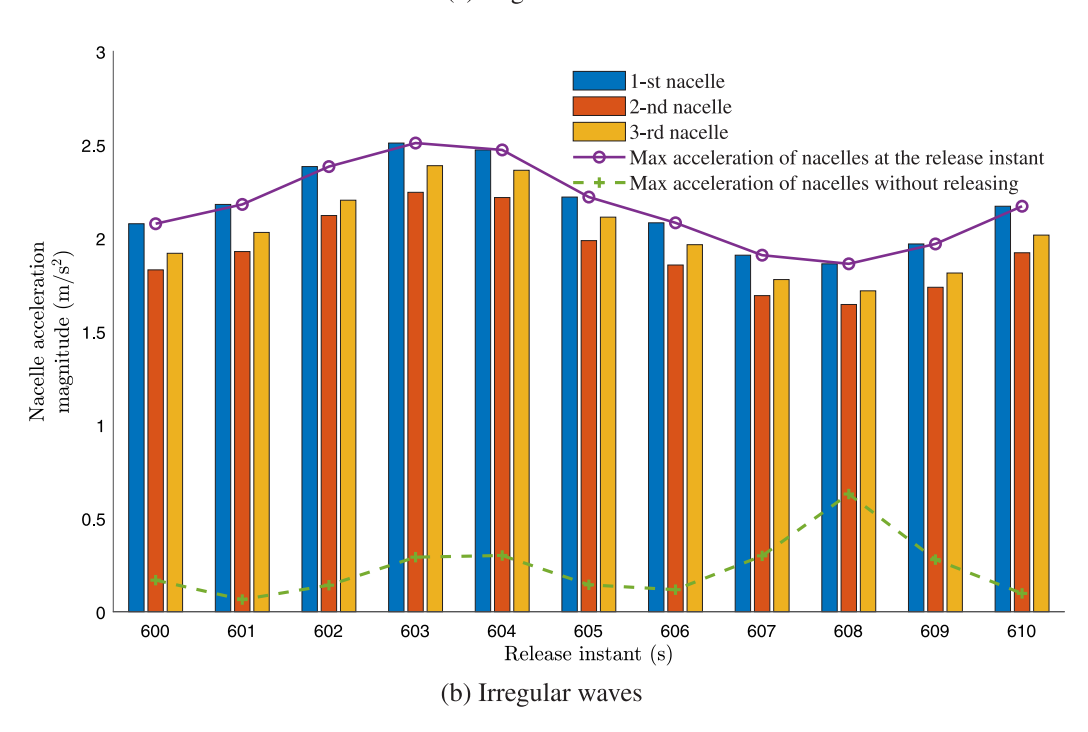


Fig. 9. Peak accelerations of the nacelles at different release instants in (a) regular waves and (b) irregular waves.

longitudinal tilt angle of 1.5 deg. This is consistent with reality, which demonstrates the rationality of this simulation and system modeling.

To more intuitively illustrate the importance of decision-making regarding the release instants in the FOWT preassembly loadoff scenario, the corresponding pre-simulations were conducted to illustrate the effects of different payload release instants on the acceleration of the FOWT nacelles.

The simulation results using different release instants and specific regular waves (wave height H=1 m, wave period T=10 s, and wave direction $\epsilon=0$ rad) are shown in Fig. 8. To avoid the effects of initialization, the results in the initial 500 s were removed. The acceleration magnitude of the nacelle placed in the middle of the vessel dock $\ddot{p}_{n,2}^n$ is presented in Fig. 8(a). The selected payload release instants in the simulations were 600 s, 654 s, and 708 s, covering

different time instants within a 10-second time interval, across different wave periods. Selection of the release time instants led to a noticeable difference in the acceleration of the onboard nacelles. Hence, intelligent decision-making support for the payload release is necessary.

The practical offshore environment is more complex. In addition to regular waves, irregular long-crested waves generated by the Jonswap spectrum were used to provide a more complex scenario. Different payload transfer instants ranging from 600 s to 610 s, at intervals of 1 s, were compared for regular waves and an irregular sea state (significant wave height H_s = 1.5 m, peak period T_p = 10 s, and wave direction ϵ = 0 rad).

The peak nacelle accelerations at different payload release instants are shown in Fig. 9. The results demonstrated that the acceleration

Table 2
Environmental parameters for regular waves and the corresponding simulation results.

EC	H(m)	T(s)	Max acceleration magnitude without PTTS (m/s²)	Acceleration magnitude with PTTS (m/s²)	Acceleration magnitude reduction ratio (%)
1	1.12	11.4	2.84	1.60	43.7
2	0.98	9.80	2.32	1.54	33.6
3	1.19	8.99	3.12	1.44	53.8
4	0.80	10.9	2.71	1.75	35.4
5	0.83	8.97	2.83	1.60	43.5
6	1.19	9.93	3.11	1.48	52.4
7	0.69	10.5	2.69	1.69	37.2
8	0.58	9.48	2.65	1.79	32.5
9	0.55	10.3	2.61	1.77	32.2
10	0.75	11.5	2.62	1.57	40.1

magnitude of the nacelles varied considerably at different release instants. The peak acceleration magnitudes of the nacelles were close to $1~\text{m/s}^2$ when the payload was not released, and reached $1.5~\text{to}~3~\text{m/s}^2$ after payload transfer. Moreover, the choice of different payload release instants resulted in up to a $1.5~\text{m/s}^2$ difference in acceleration magnitude. The difference was mainly due to the wave loads generated at the payload transfer instant. Hence, decision-making support regarding the payload release instant is necessary to fully use wave-induced loads in the opposite direction and compensate for the inertial loads caused by a sudden payload release.

In Fig. 9, it is noted that the effects of inertia load reduction in irregular waves are less effective than those in regular waves, although the energy of the irregular waves is higher. The main reason is that irregular waves consist of multiple harmonic wave components with different initial phases, which are determined by the selection of random seeds. Since the total wave loads are considered the superposition of the loads arising from these components, the magnitudes of the total wave loads may be amplified or reduced due to the phase difference among wave components. Compared to the case in regular waves, the load magnitudes were reduced in the irregular waves. Hence, there was a performance inferiority in the proposed case studies.

The acceleration magnitude at the second nacelle was the least among the three. This was mainly due to the nacelle in the middle of the vessel having a slightly lower lever arm than the vessel's center of gravity.

4.3. Decision-making for payload release instant

For the sea states (1) regular waves: wave height H=1 m, wave period T=10 s, and wave direction $\epsilon=0$ rad and (2) irregular waves: significant wave height $H_s=1.5$ m, peak period $T_p=10$ s, and wave direction $\epsilon=0$ rad, the decision-making phase started at 600 s. The nacelle acceleration threshold \overline{a} was set to 1.6 m/s² to validate the control algorithm. If a high nacelle acceleration threshold \overline{a} was set, the release conditions can be easily satisfied. On the contrary, if the value was low, the payload was not released even under certain relatively safe conditions. In practice, extensive experimental verification is required to determine the threshold value.

The decision results for the payload release instants were 604.5 s and 616.5 s for the regular and irregular waves, respectively. The acceleration magnitudes for the onboard nacelles reached 1.52 and 1.74 m/s 2 , respectively. The time-domain results from 550 to 650 s are presented in Fig. 10. Results of uncontrolled releases at 600–610 s (sampling interval of 1 s) were marked as purple scatters. Each point denoted the peak wind turbine nacelle acceleration magnitude after release at the specific release time instant. The maximum peak acceleration magnitude for the onboard nacelles after release time instant decided by the PTTS algorithm was smaller than those without control. It was summarized that the proposed PTTS algorithm was effective in limiting the max nacelle acceleration after the payload release.

The acceleration magnitudes at the nacelle were greater than at the threshold. Only two DOF motions (i.e., heave and pitch) were considered in the threshold, but actually there were six DOF motions in the simulations. To further ensure the safety of the release process, a safety factor is recommended to increase the basis of the release threshold (i.e., $\max_j(|\vec{p}_{n,j}^n(t_r^*)|) \leqslant \gamma \overline{a}$, where $\gamma \in (0,1)$). Other decision-making strategies (i.e., the Bayesian method) can be a great paradigm to improve performance and accuracy.

4.4. Ballast tank control after release

The inertial load reduction algorithm is carried out in the regular and irregular waves, respectively. The simulation results from 500 s to 800 s are presented in Fig. 11.

The APBC algorithm effectively received the signal regarding whether the payload was released and began controlling the individual pumps' inlet and outlet flow rates. Compared to the results for only executing a preassembly loadoff, the proposed active ballast control algorithm effectively reduced the acceleration magnitude at the nacelles. Moreover, the acceleration magnitude could be maintained at a relatively low level during execution of the APBC algorithm. In addition, the mean pitch motion was decreased by using the ballast tanks (see Figs. 11(e) and 11(f)).

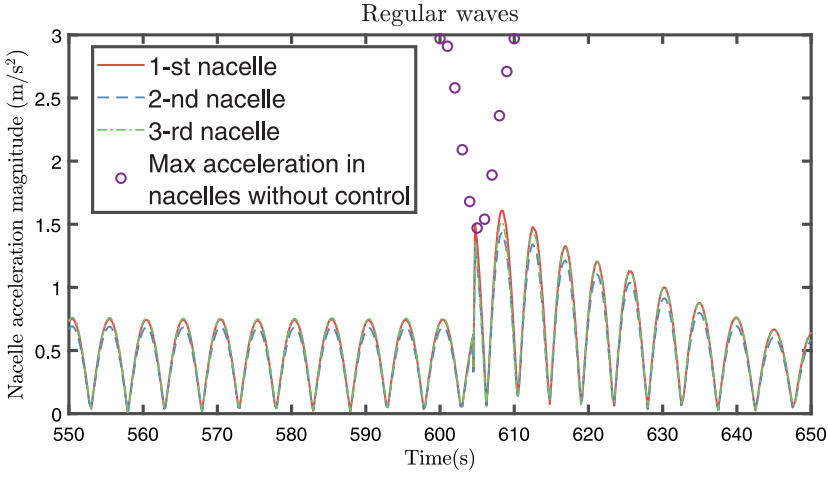
Noteworthy, the system design is still under conceptual research, and the max flow rates of the pumps are set to be somewhat larger than normal. In applications, a higher flow rate of the pumps can provide better anti-pitch effects. Furthermore, once the ballast tank is filled, the anti-pitch performance deteriorate significantly. Therefore, the vessel and mechanical designs are coupled, which should be further investigated in future research.

4.5. Algorithm validation

Monte Carlo simulations were conducted to evaluate the effectiveness of the proposed algorithms, a total of 10 simulations for regular wave random environmental conditions (ECs) and 10 simulations for irregular wave random ECs. The wave parameters included the wave height H and wave period T for the regular waves, and significant wave height H_s and peak period T_p for the irregular waves. The wave direction ϵ was set at 0, and the allowable release threshold \overline{a} for both wave environments was set at 1.6 m/s². A 800-second time-domain simulation was conducted under each EC.

To avoid redundancy, the time domain simulation results were not presented. The wave parameters and corresponding simulation results are listed in Tables 2 and 3. The results verify the robustness of the proposed algorithms. The acceleration magnitudes in the nacelles were reduced by a minimum of 30%. In specific sea states, the acceleration magnitude reduction was significant: 53.8% in EC 3 (regular waves) and 47.2% in EC 7 (irregular waves).

The selection of \overline{a} was critical. Excessively liberal release conditions created the risk of damage to the internal mechanisms of the onboard nacelles. Overly strict release conditions, in turn, made it difficult to meet the release conditions for the preassembly and extend the time of offshore operations for FOWT installation. Therefore, a certain amount



(a) Release instant selection for regular waves

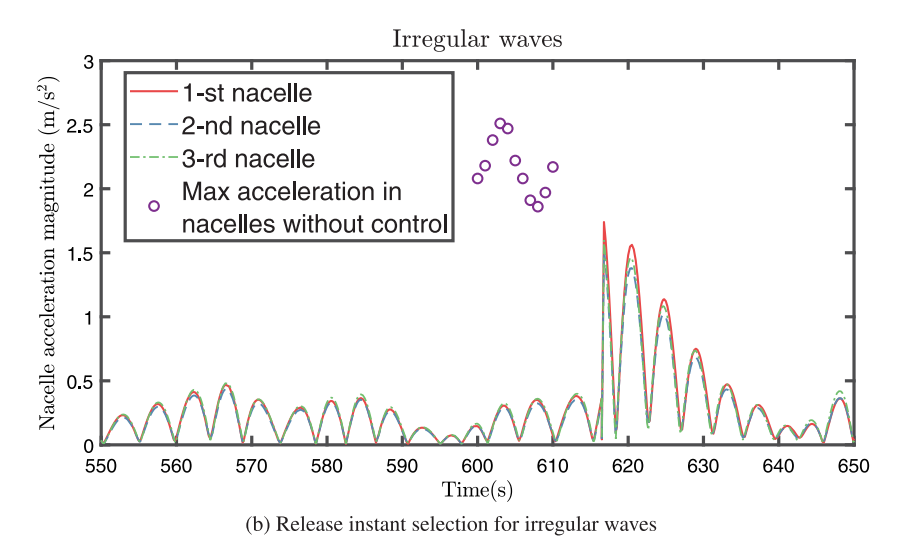


Fig. 10. Effects of the PTTS algorithm for (a) regular and (b) irregular waves.

Table 3

Environmental parameters for irregular waves and the corresponding simulation results.

EC	$H_s(\mathbf{m})$	$T_p(\mathbf{s})$	Max acceleration magnitude without PTTS (m/s²)	Acceleration magnitude with PTTS (m/s ²)	Acceleration magnitude reduction ratio (%)
1	1.33	11.3	2.68	1.71	36.2
2	1.21	11.5	2.54	1.73	31.9
3	1.46	10.6	2.75	1.54	44.0
4	1.29	8.89	2.73	1.68	38.5
5	1.59	9.68	2.83	1.52	46.3
6	1.19	11.0	2.55	1.58	38.0
7	1.57	10.7	2.82	1.49	47.2
8	1.15	10.3	2.61	1.57	39.8
9	1.45	9.02	2.80	1.77	36.8
10	1.62	10.3	2.82	1.68	40.4

of simulation and scaled model experiments are necessary for setting up nacelle acceleration safety threshold $\bar{a}.$

It is worth noting that the use of different types of vessels as the installation vessel had different effects. Using a smaller displacement vessel made the inertial load reduction algorithm more effective at reducing the maximum acceleration magnitude of the nacelle. Moreover, vessels with a greater waterline area (e.g., catamarans, trimarans) made the release process more stable. The payload released on the side of the vessel caused a more substantial roll motion after the payload was released. Thus, this installation method required support from the inertial load reduction algorithm.

5. Conclusion

Substantial inertial loads after payload release are a challenge for the tower–nacelle–rotor preassembly installation. This work proposed a method for reducing inertial loads after the payload transfer. The scheme consisted of two parts: a release time decision-making algorithm and anti-pitch ballast controller. The numerical simulation results using a 6DOF model showed that the algorithms designed according to the proposed 2DOF simplified model were able to calculate the optimal payload release time instant for long-crested waves. Moreover, the controller effectively scheduled ballast water to reduce the mean

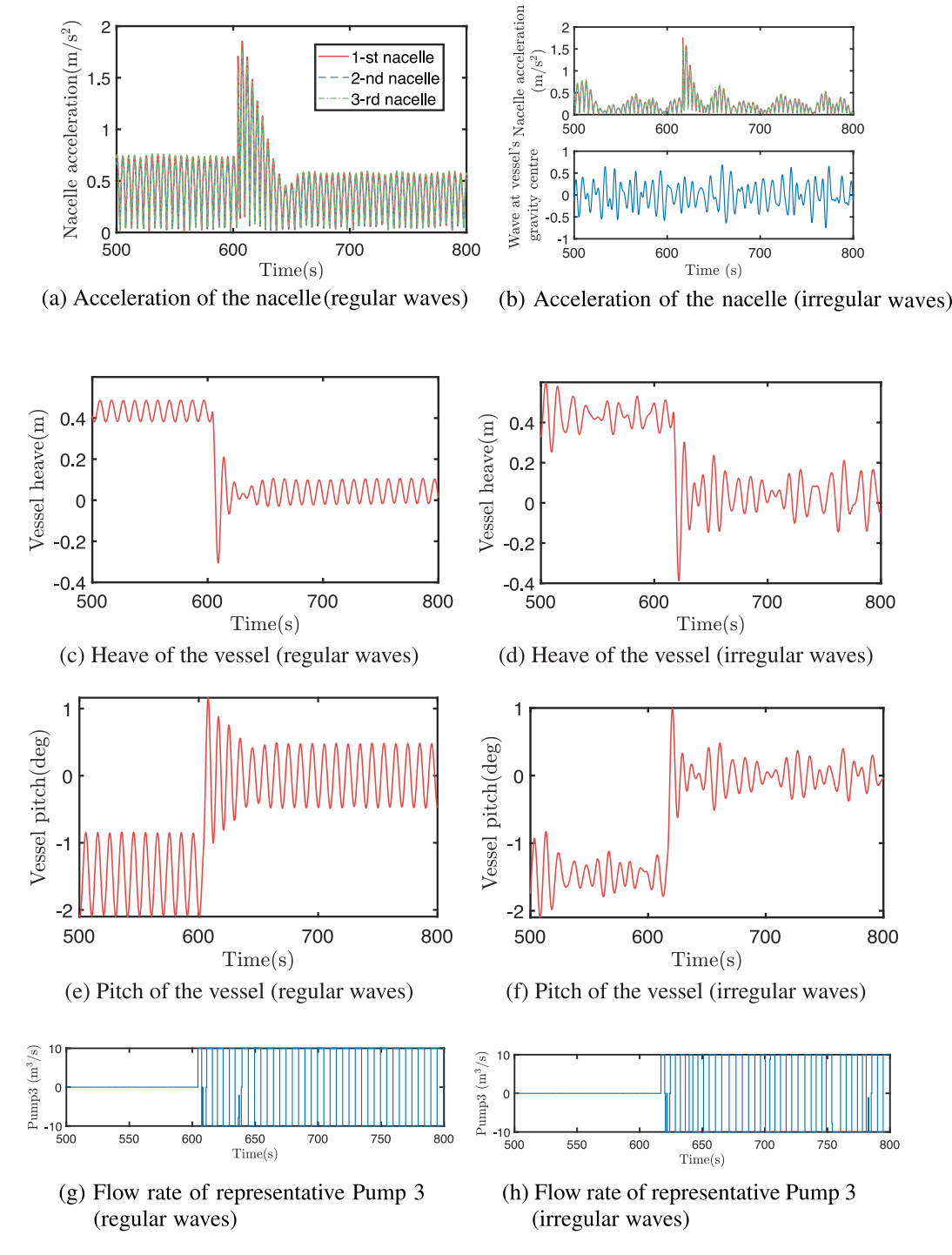


Fig. 11. Combination of PTTS and APBC algorithms for regular and irregular waves.

acceleration of the onboard nacelles after release. The peak acceleration magnitudes of onboard nacelles after the loadoff instant were limited, effectively protecting the mechanism in the nacelles.

To further enhance the applicability of the proposed algorithms, more complex marine environments will be considered for the control, such as short-crested waves and swell. In addition, gust wind may also play an important role in the inertial load, which makes the control tougher. Instead of a two DOF control object, anti-roll and anti-pitch control should be further integrated using a catamaran installation vessel. Future research on complex system dynamics and the interaction among mechanical components is necessary to improve the understanding of its operational criteria. The strength of the connectors also

needs to be analyzed and verified. Furthermore, more accurate wave elevation estimation and wave-load prediction techniques should be further investigated. State-of-the-art decision-making methods can be further studied to improve the performance.

CRediT authorship contribution statement

Can Ma: Writing – original draft, Methodology, Software. Zhen-Zhong Hu: Writing – review & editing. Xiang Yuan Zheng: Writing – review & editing. Zhengru Ren: Conceptualization, Methodology, Writing – review & editing, Funding acquisition.

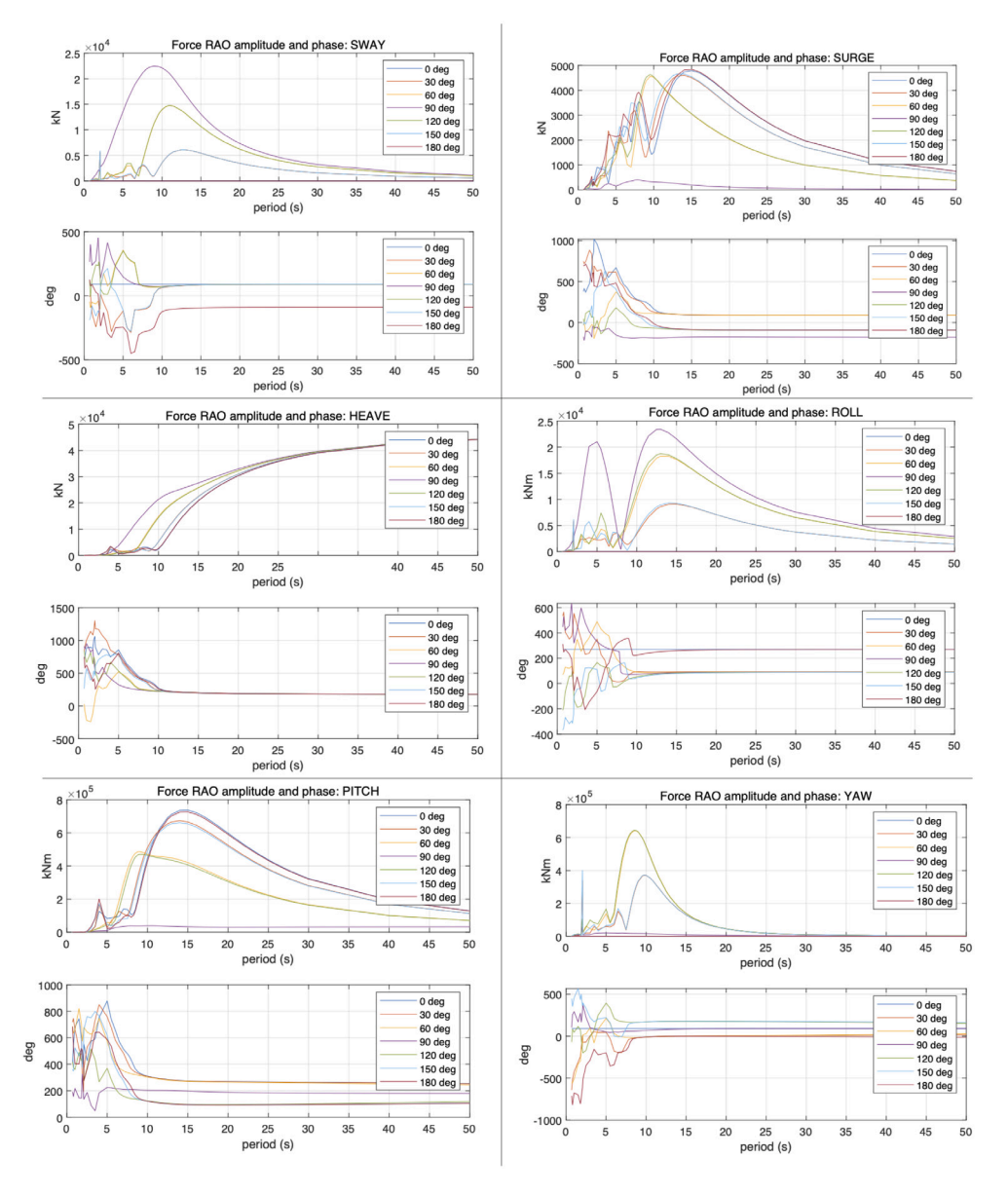


Fig. 12. Force RAO amplitude and phase of the installation used in simulation.

Declaration of competing interest

The authors declare that they have no known competing financial interests or personal relationships that could have appeared to influence the work reported in this paper.

Acknowledgments

This work was supported by the Wenhai Program of QNLM, Shenzhen Science and Technology Program (KJZD20231023100459001), the Key Promotion Program of High Quality Marine Economy Development by Guangdong Province of China (GDNRC [2022] 33), the Major Program of Stable Sponsorship for Higher Institutions (Shenzhen Science & Technology Commission, WDZC20200819174646001), and the Guangdong Basic and Applied Basic Research Foundation (2022B1515130006).

Appendix

The force RAO of the installation used in the simulation is calculated by Wamit, shown in Fig. 12.

References

Andersson, J.A.E., Gillis, J., Horn, G., Rawlings, J.B., Diehl, M., 2019. CasADi: a software framework for nonlinear optimization and optimal control. Math. Program. Comput. 11 (1), 1–36. http://dx.doi.org/10.1007/s12532-018-0139-4.

Ataei, B., Yuan, S., Ren, Z., Halse, K.H., 2023. Effects of structural flexibility on the dynamic responses of low-height lifting mechanism for offshore wind turbine installation. Mar. Struct. 89, 103399. http://dx.doi.org/10.1016/j.marstruc.2023.103399, URL https://www.sciencedirect.com/science/article/pii/S0951833923000321.

Barlow, E., Oeztuerk, D.T., Revie, M., Boulougouris, E., Day, A.H., Akartunali, K., 2015. Exploring the impact of innovative developments to the installation process for an offshore wind farm. Ocean Eng. 109, 623–634. http://dx.doi.org/10.1016/j.oceaneng.2015.09.047.

Bhardwaj, U., Teixeira, A., Soares, C.G., 2019. Reliability prediction of an off-shore wind turbine gearbox. Renew. Energy 141, 693–706. http://dx.doi.org/10. 1016/j.renene.2019.03.136, URL https://www.sciencedirect.com/science/article/pii/S0960148119304574.

Borge, J., Rodriguez, G., Hessner, K., Gonzalez, P., 2004. Inversion of marine radar images for surface wave analysis. J. Atmos. Ocean. Technol. 21 (8), 1291–1300.

C. Ma et al. Sustainable Horizons 10 (2024) 100096

Castro-Santos, L., Martins, E., Guedes Soares, C., 2016. Cost assessment methodology for combined wind and wave floating offshore renewable energy systems. Renew. Energy 97, 866–880. http://dx.doi.org/10.1016/j.renene.2016.06.016.

- Dai, Y., Gao, H., Yu, S., Ju, Z., 2022. A fast tube model predictive control scheme based on sliding mode control for underwater vehicle-manipulator system. Ocean Eng. 254, 111259. http://dx.doi.org/10.1016/j.oceaneng.2022.111259, URL https: //www.sciencedirect.com/science/article/pii/S0029801822006539.
- Du, J., Hu, X., Krstic, M., Sun, Y., 2016. Robust dynamic positioning of ships with disturbances under input saturation. Automatica 73, 207–214. http://dx.doi.org/ 10.1016/j.automatica.2016.06.020.
- Fang, M.-C., Zhuo, Y.-Z., Lee, Z.-Y., 2010. The application of the self-tuning neural network PID controller on the ship roll reduction in random waves. Ocean Eng. 37 (7), 529–538. http://dx.doi.org/10.1016/j.oceaneng.2010.02.013, URL https://www.sciencedirect.com/science/article/pii/S0029801810000582.
- Feng, N., Wu, D., Yu, H., Yamashita, A.S., Huang, Y., 2022. Predictive compensator based event-triggered model predictive control with nonlinear disturbance observer for unmanned surface vehicle under cyber-attacks. Ocean Eng. 259, 111868. http:// dx.doi.org/10.1016/j.oceaneng.2022.111868, URL https://www.sciencedirect.com/ science/article/pii/S0029801822012100.
- Fossen, T.I., 2011. Handbook of Marine Craft Hydrodynamics and Motion Control. John Wiley & Sons.
- Gan, L., Yan, Z., Zhang, L., Liu, K., Zheng, Y., Zhou, C., Shu, Y., 2022. Ship path planning based on safety potential field in inland rivers. Ocean Eng. 260, 111928. http://dx.doi.org/10.1016/j.oceaneng.2022.111928, URL https://www.sciencedirect.com/science/article/pii/S0029801822012665.
- Gao, S., Liu, C., Tuo, Y., Chen, K., Zhang, T., 2022. Augmented model-based dynamic positioning predictive control for underactuated unmanned surface vessels with dual-propellers. Ocean Eng. 266, 112885. http://dx.doi.org/10.1016/ j.oceaneng.2022.112885, URL https://www.sciencedirect.com/science/article/pii/ S0029801822021680.
- Han, Y., Le, C., Ding, H., Cheng, Z., Zhang, P., 2017. Stability and dynamic response analysis of a submerged tension leg platform for offshore wind turbines. Ocean Eng. 129, 68–82. http://dx.doi.org/10.1016/j.oceaneng.2016.10.048, URL https://www.sciencedirect.com/science/article/pii/S0029801816304954.
- Hu, Z., Li, X., Zhao, W., Wu, X., 2017. Nonlinear dynamics and impact load in float-over installation. Appl. Ocean Res. 65, 60–78. http://dx.doi.org/10.1016/j.apor.2017.03. 013.
- Jiang, Z., 2021. Installation of offshore wind turbines: A technical review. Renew. Sustain. Energy Rev. 139, 110576. http://dx.doi.org/10.1016/j.rser.2020.110576, URL https://www.sciencedirect.com/science/article/pii/S1364032120308601.
- Jiang, Z., Li, L., Gao, Z., Halse, K.H., Sandvik, P.C., 2018. Dynamic response analysis of a catamaran installation vessel during the positioning of a wind turbine assembly onto a spar foundation. Mar. Struct. 61, 1–24. http://dx.doi.org/10.1016/ i.marstruc.2018.04.010.
- Le, C., Ren, J., Wang, K., Zhang, P., Ding, H., 2021. Towing performance of the submerged floating offshore wind turbine under different wave conditions. J. Mar. Sci. Eng. 9 (6), http://dx.doi.org/10.3390/jmse9060633, URL https://www.mdpi. com/2077-1312/9/6/633.
- Li, X., Zhao, H., Deng, W., 2023. BFOD: Blockchain-based privacy protection and security sharing scheme of flight operation data. IEEE Internet Things J..
- Lin, L., Li, S., Huo, L., Liu, X., 2023. Study on the relationship between fractal dimension and particle fragmentation for marine coral sand under impact load. Ocean Eng. 286, 115442.
- Liu, T., Halse, K.H., Leira, B.J., Jiang, Z., 2023a. Comparative study of the mating process for a spar-type floating wind turbine using two alternative installation vessels. Appl. Ocean Res. 132, http://dx.doi.org/10.1016/j.apor.2022.103452.
- Liu, C., Hu, Q., Wang, X., Yin, J., 2022. Event-triggered-based nonlinear model predictive control for trajectory tracking of underactuated ship with multi-obstacle avoidance. Ocean Eng. 253, 111278. http://dx.doi.org/10.1016/ j.oceaneng.2022.111278, URL https://www.sciencedirect.com/science/article/pii/ S0029801822006722
- Liu, Y., Zhang, J.-M., Min, Y.-T., Yu, Y., Lin, C., Hu, Z.-Z., 2023b. A digital twin-based framework for simulation and monitoring analysis of floating wind turbine structures. Ocean Eng. 283, 115009.
- Lu, Z., 2013. Study and development on safety operation of marine pump. In: Wu, J., Lu, X., Xu, H., Nakagoshi, N. (Eds.), Resources and Sustainable Development, PTS 1-4. In: Advanced Materials Research, vol. 734–737, Inner Mongolia Univ; Chinese Acad Sci, Res Ctr Eco Environm Sci, Key Lab Environm Biotechnol, pp. 2681–2684. http://dx.doi.org/10.4028/www.scientific.net/AMR.734-737.2681, 2nd International Conference on Energy and Environmental Protection (ICEEP 2013), Guilin, PEOPLES R CHINA, APR 19-21, 2013.
- Ma, X., Huang, L., Duan, W., Jing, Y., Zheng, Q., 2021. The performance and optimization of ANN-WP model under unknown sea states. Ocean Eng. 239, http: //dx.doi.org/10.1016/j.oceaneng.2021.109858.

- Ma, H., Zhang, Y., Wang, S.-Q., Xu, J., Su, H., 2022. Rolling-optimized model predictive vibration controller for offshore platforms subjected to random waves and winds under uncertain sensing delay. Ocean Eng. 252, 111054. http:// dx.doi.org/10.1016/j.oceaneng.2022.111054, URL https://www.sciencedirect.com/ science/article/pii/S0029801822004644.
- Mayne, D.Q., 2014. Model predictive control: Recent developments and future promise. Automatica 50 (12), 2967–2986. http://dx.doi.org/10.1016/j.automatica.2014.10. 128, URL https://www.sciencedirect.com/science/article/pii/S0005109814005160.
- Messineo, S., Serrani, A., 2009. Offshore crane control based on adaptive external models. Automatica 45 (11), 2546–2556. http://dx.doi.org/10.1016/j.automatica. 2009.07.032.
- Rakibuzzaman, M., Kim, H.H., Kim, K.W., Suh, S.H., Bae, Y.S., 2022. A study on booster pump system with flow sensor for individual flow control method. J. Appl. Fluid Mech. 15 (3), 889–900. http://dx.doi.org/10.47176/jafm.15.03.33153.
- Ren, Z., Han, X., Yu, X., Skjetne, R., Leira, B.J., Saevik, S., Zhu, M., 2023a. Data-driven simultaneous identification of the 6DOF dynamic model and wave load for a ship in waves. Mech. Syst. Signal Process. 184, http://dx.doi.org/10.1016/j.ymssp.2022. 109422.
- Ren, Z., Jiang, Z., Skjetne, R., Gao, Z., 2018. Development and application of a simulator for offshore wind turbine blades installation. Ocean Eng. 166, 380–395. http://dx.doi.org/10.1016/j.oceaneng.2018.05.011, URL https://www.sciencedirect.com/science/article/pii/S0029801818307224.
- Ren, Z., Skjetne, R., Gao, Z., 2019. A crane overload protection controller for blade lifting operation based on model predictive control. Energies 12 (1), http://dx.doi. org/10.3390/en12010050, URL https://www.mdpi.com/1996-1073/12/1/50.
- Ren, Z., Skjetne, R., Verma, A.S., Jiang, Z., Gao, Z., Halse, K.H., 2021a. Active heave compensation of floating wind turbine installation using a catamaran construction vessel. Mar. Struct. 75, http://dx.doi.org/10.1016/j.marstruc.2020.102868.
- Ren, Z., Verma, A.S., Ataei, B., Halse, K.H., Hildre, H.P., 2021b. Model-free antiswing control of complex-shaped payload with offshore floating cranes and a large number of lift wires. Ocean Eng. 228, 108868. http://dx.doi.org/10.1016/j.oceaneng.2021.108868, URL https://www.sciencedirect.com/science/article/pii/S0029801821003036.
- Ren, Z., Zhen, X., Jiang, Z., Gao, Z., Li, Y., Shi, W., 2023b. Underactuated control and analysis of single blade installation using a jackup installation vessel and active tugger line force control. Mar. Struct. 88, http://dx.doi.org/10.1016/j.marstruc. 2022.103338.
- Shah, K.A., Li, Y., Nagamune, R., Zhou, Y., Ur Rehman, W., 2021. Platform motion minimization using model predictive control of a floating offshore wind turbine. Theor. Appl. Mech. Lett. 11 (5), 100295. http://dx.doi.org/10.1016/j.taml.2021.100295, URL https://www.sciencedirect.com/science/article/pii/S2095034921001021.
- Shen, C., Shi, Y., Buckham, B., 2017. Integrated path planning and tracking control of an AUV: A unified receding horizon optimization approach. IEEE/ASME Trans. Mechatronics 22 (3), 1163–1173. http://dx.doi.org/10.1109/TMECH.2016. 2612689.
- Shen, C., Shi, Y., Buckham, B., 2019. Path-following control of an AUV: A multiobjective model predictive control approach. IEEE Trans. Control Syst. Technol. 27 (3), 1334–1342. http://dx.doi.org/10.1109/TCST.2018.2789440.
- Sun, X., Huang, D., Wu, G., 2012a. The current state of offshore wind energy technology development. Energy 41 (1), 298–312. http://dx.doi.org/10.1016/j.energy.2012.02. 054, 23rd International Conference on Efficiency, Cost, Optimization, Simulation and Environmental Impact of Energy Systems (ECOS), Lausanne, SWITZERLAND, 2010.
- Sun, Q., Zhang, M., Zhou, L., Garme, K., Burman, M., 2022. A machine learning-based method for prediction of ship performance in ice: Part I. ice resistance. Mar. Struct. 83, 103181.
- $Ulstein,\ 2021.\ Windlifter.\ URL\ https://ulstein.com/equipment/ulstein-windlifter.$
- Verma, A.S., Vedvik, N.P., Gao, Z., 2019. A comprehensive numerical investigation of the impact behaviour of an offshore wind turbine blade due to impact loads during installation. Ocean Eng. 172, 127–145. http://dx.doi.org/10.1016/ j.oceaneng.2018.11.021, URL https://www.sciencedirect.com/science/article/pii/ S0029801818321024
- Wang, X., Li, S., Liu, Q., Liu, Z., 2022. Sequential matching optimization for lifting trajectory and ballast water allocation of the intelligent revolving floating crane. Ocean Eng. 266 (5), http://dx.doi.org/10.1016/j.oceaneng.2022.113061.
- Wu, X., Hu, Y., Li, Y., Yang, J., Duan, L., Wang, T., Adcock, T., Jiang, Z., Gao, Z., Lin, Z., Borthwick, A., Liao, S., 2019. Foundations of offshore wind turbines: A review. Renew. Sustain. Energy Rev. 104, 379–393. http://dx.doi.org/10.1016/j.rser.2019.01.012
- Yan, C., Wang, H., Guo, Y., Wang, Z., Liu, X., 2021. Laboratory study of integrated wet-towing of a triple-bucket jacket foundation for far-offshore applications. J. Mar. Sci. Eng. 9 (11), http://dx.doi.org/10.3390/jmse9111152, URL https://www.mdpi. com/2077-1312/9/11/1152.
- Zeng, X., Shi, W., Feng, X., Shao, Y., Li, X., 2023. Investigation of higher-harmonic wave loads and low-frequency resonance response of floating offshore wind turbine under extreme wave groups. Mar. Struct. 89, 103401.

Zhang, P., Han, Y., Ding, H., Zhang, S., 2015. Field experiments on wet tows of an integrated transportation and installation vessel with two bucket foundations for offshore wind turbines. Ocean Eng. 108, 769–777. http://dx.doi.org/10.1016/ j.oceaneng.2015.09.001, URL https://www.sciencedirect.com/science/article/pii/ S0029801815004667.

Zhang, M., Hao, S., Wu, D., Chen, M.-L., Yuan, Z.-M., 2022. Time-optimal obstacle avoidance of autonomous ship based on nonlinear model predictive control. Ocean Eng. 266, 112591. http://dx.doi.org/10.1016/j.oceaneng.2022.112591, URL https://www.sciencedirect.com/science/article/pii/S0029801822018741.

Zhao, S., Gao, Z., Meng, X., Li, H., 2023. Multibody coupled dynamic response analysis of a dual barge float-over operation system with motion compensation equipment under a passive operational mode. Ocean Eng. 269, 113499. http://dx.doi.org/10. 1016/j.oceaneng.2022.113499.



Can Ma received his B.Eng. degree from Chongqing Jiaotong University in 2017. He is currently pursuing the M.S. degree at Institute for Ocean Engineering, Shenzhen International Graduate School, Tsinghua University. His research interests include offshore wind energy, marine operations, marine control system, and ocean engineering.



Assist. Prof. Dr. Zhengru Ren received a B.Eng. degree in Ocean Engineering from the Dalian University of Technology, Dalian, China, in 2012, and the M.Sc. and Ph.D. degrees in Marine Technology from the Norwegian University of Science and Technology (NTNU), Trondheim, Norway, in 2015 and 2019, respectively. From 2019 to 2021, he was a Postdoctoral research fellow with the Centre for Research-based Innovation on Marine Operations (SFI MOVE), Department of Marine Technology, NTNU. Since 2022, he has been an Assistant Professor at the Institute for Ocean Engineering, Tsinghua University, China. His research interests are within nonlinear control theory, sensor fusion, intelligent and digitalized ocean engineering, and offshore wind energy. He has published more than 50 scientific papers in international journals and conferences and received 13 granted patients. In 2021, he received the National Science Foundation for Excellent Young Scholars (Overseas).